First-principles study on surface stability and interface magnetic properties of SmFe$_{12}$

Yuta Ainai[1] , Tomoharu Shiozawa[1], Yasutomi Tatetsu[1,2], and Yoshihiro Gohda[1]*

[1]Department of Materials Science and Engineering, Tokyo Institute of Technology, Yokohama 226-8502, Japan
[2]University Center for Liberal Arts Education, Meio University, Nago 905-8585, Japan

*E-mail: gohda.y.ab@m.titech.ac.jp

We report the most stable surface of SmFe$_{12}$ and the interface magnetic properties of SmFe$_{12}$ with SmCu and bcc Fe as subphases. We find that the (110) surface with the highest exposition of Sm is the most stable surface of SmFe$_{12}$. Stabilization by the exposition of rare-earth is also confirmed for Nd$_2$Fe$_{14}$B. Moreover, we also demonstrate that SmCu improves not only magnetic moments and the anisotropy of grain surfaces of SmFe$_{12}$ but also well suppresses the magnetic interaction between SmFe$_{12}$ grains. © 2020 The Japan Society of Applied Physics

Ferromagnetic rare-earth compounds with the tetragonal ThMn$_{12}$ structure have been seen as a promising main phase of permanent magnets becoming a successor to Nd$_2$Fe$_{14}$B, due to their magnetic properties comparable with or exceeding those of Nd$_2$Fe$_{14}$B.[1–3] In particular, among RFe$_{12}$ (R: rare-earth element) compounds, the samarium-based compound SmFe$_{12}$ with a particularly large anisotropy field[4–6] is a potential candidate for the main phase of permanent magnets. However, the binary SmFe$_{12}$ compound has a problem that the bulk phase is thermodynamically unstable.[7,8] Previous experiments reported the stability is ensured by the partial substitution of Fe atoms in SmFe$_{12}$ with nonmagnetic third elements such as Ti, V, Mn, Co, and Zn.[8–14]

On the other hand, as effects of microstructures, local magnetic properties including the anisotropy of rare-earth elements in the main phase close to interfaces are greatly affected by the physical properties of subphases, e.g. the crystal structure, the chemical composition, and the magnetism. In particular, those of the interfacial first layer are significantly different from the bulk state.[15,16] Thus, in order to realize the permanent magnets with the magnetic properties superior to the existing ones, it is necessary to understand the local magnetic properties of the interfaces on the atomic scale. Moreover, for the sake of the realization of the high coercivity, the suppression of the magnetic interaction between the main-phase grains by nonmagnetic subphases is needed.[17] The partial substitution of Fe atoms with nonmagnetic elements to stabilize SmFe$_{12}$ often causes regrettably the precipitation of ferromagnetic α-Fe.[8,14,18–20] In the case of Sm$_2$Fe$_{17}$N$_3$, recent investigations have proposed the possibility of avoiding the α-Fe precipitation by introducing Sm–Cu phases, particularly SmCu.[21] These new findings should also suppress the α-Fe precipitation for SmFe$_{12}$, due to the fact that the chemical composition of Sm$_2$Fe$_{17}$ is close to that of SmFe$_{12}$, and SmCu has been observed in computational study of the Sm–Fe–Cu phase diagram.[22] In this sense, SmCu may be a promising candidate for a subphase of Sm-based permanent magnets with SmFe$_{12}$ as the main phase.

As mentioned above, the magnetic properties of the permanent magnets are closely related to the electronic states of interfaces between the main phase and a subphase. In order to reveal the electronic states of interfaces, interfacial atomic configurations are needed. To accomplish this, it is first and foremost required to identify surface structures of main-phase grains, because microstructure interfaces are usually formed by the solidification of a subphase on surfaces of the main phase. However, such surface atomic structures of SmFe$_{12}$ as well as of Nd$_2$Fe$_{14}$B are yet to be investigated.

In this paper, we first identify the most stable atomic configurations of SmFe$_{12}$ surfaces. We find surfaces with the highest exposition of the Sm atoms is found to be most stable. Surfaces of Nd$_2$Fe$_{14}$B are also examined, and the same trend is observed. We clarify that this surface stabilization by the exposition of rare-earth atoms comes from weaker chemical bondings of 5d states of rare-earth atoms compared with those of 3d states of Fe atoms, which minimizes the loss of the band energy of d electrons. Second, we investigate the magnetic properties of SmFe$_{12}$(110)/SmCu(100) and SmFe$_{12}$(110)/Fe(001) interfaces. We find that SmCu enhances the magnetic moments of the main-phase Fe atoms located near the interface to approximately 2.49 μ_B. The reason for this enhancements is a decrease in the hybridization between 3d states of the Fe atoms compared with that of the SmFe$_{12}$ bulk, which is combined with the charge neutrality for 3d states of the Fe atoms. The improvement of the anisotropy of Sm atoms at interfaces are also observed. In addition, we quantitatively evaluated the effective exchange-coupling constant between the main-phase grains. The results show that SmCu well suppresses the magnetic interaction between the main-phase grains compared with ferromagnetic α-Fe.

Our first-principles calculations of surfaces and interfaces are based on density function theory using pseudopotentials and pseudo-atomic-orbital basis functions as implemented in the OpenMX code.[23] In all calculations, the Perdew–Burke–Ernzerhof exchange-correlation functional[24] within the generalized-gradient approximation was adopted. As basis sets, $s2p2d2$ configurations were used for Sm, Nd, Fe, Cu, and B with cutoff radii of 8.0, 8.0, 6.0, 6.0, and 7.0 Bohr, respectively. Semicore orbitals of 3s and 3p in Fe and Cu as well as 5s and 5p in Sm and Nd were treated as valence electrons. Open-core pseudopotentials were used for Sm and Nd atoms, where 4f electrons were treated as spin-polarized core electrons. As for convergence criteria, the maximum

force on each atom and the total-energy variation are 10^{-4} Hartree/Bohr and 3.1×10^{-9} Hartree/atom for surface calculations, and 10^{-3} Hartree/Bohr and 1.3×10^{-7} Hartree/atom for interface calculations, respectively. The lattice parameters were set to $a = b = 8.54$ Å and $c = 4.71$ Å for SmFe$_{12}$, $a = b = 8.79$ Å and $c = 12.14$ Å for Nd$_2$Fe$_{14}$B, $a = 7.38$, $b = 4.56$ Å, and $c = 5.64$ Å for FeB type SmCu, and $a = b = c = 2.84$ Å for bcc Fe obtained by our calculations, respectively. Collinear spin structures neglecting the spin–orbit coupling of the valence electrons are considered with the energy cutoff of 500 Ry. The k-point grids of

$8 \times 8 \times 14$ for SmFe$_{12}$ and $8 \times 8 \times 6$ for Nd$_2$Fe$_{14}$B unit cell were adopted, respectively, where the k-point grids for surfaces and interfaces were scaled according to their lattice parameters. The initial spin configuration has the antiparallel structure between a rare-earth element and Fe.

First, we discuss the energetic stability of rare-earth-compound surfaces. The surfaces are represented as repeated slab models, and separated by 10 Å as the vacuum gap. In the case of SmFe$_{12}$ surfaces, the surface-energy density γ is evaluated by
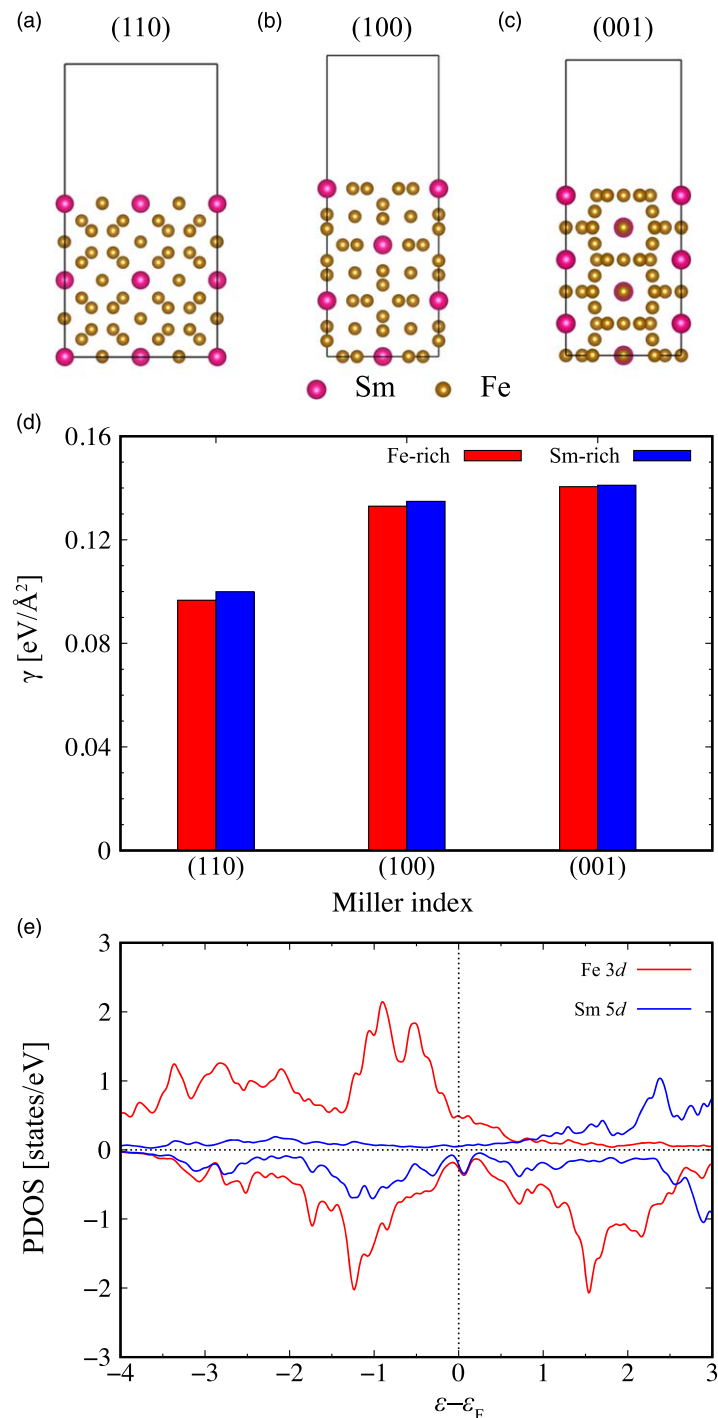
Fig. 1. (Color online) (a)–(c) Surface structures and (d) surface-energy densities γ of SmFe$_{12}$. (e) Projected density of states (PDOS) for $5d$ states of the Sm atoms and $3d$ states of the Fe atoms in the SmFe$_{12}$ bulk. The upper (lower) panel denotes the PDOS of the majority (minority) spin, respectively. The single-electron energy is defined relative to the Fermi energy ε_F.

$$\gamma = \frac{E_{\text{slab}} - (N_{\text{Sm}}\mu_{\text{Sm}} + N_{\text{Fe}}\mu_{\text{Fe}})}{2A} \quad (1)$$

with the constraint of

$$E_{\text{SmFe}_{12}} = \mu_{\text{Sm}} + 12\mu_{\text{Fe}}, \quad (2)$$

where E_{slab} is the total energy of the surface slab, N_i is the number of atoms for the element i within the slab, μ_i is the chemical potential of the element i, A is the surface area, and $E_{\text{SmFe}_{12}}$ is the total energy of the SmFe$_{12}$ bulk per formula unit. In the Fe-rich condition, we use $\mu_{\text{Fe}} = \mu_{\text{bcc-Fe}}$ meaning that SmFe$_{12}$ is equilibrium with bcc Fe. In this case, μ_{Sm} is obtained by Eq. (2). Likewise, the Sm-rich condition is considered by $\mu_{\text{Sm}} = \mu_{\alpha\text{-Sm}}$ meaning that SmFe$_{12}$ is equilibrium with α-Sm.

The surfaces of SmFe$_{12}$ with the Miller indices of (110), (100) and (001) are calculated for all possible 14 terminations, and we discuss only the most stable surface for each Miller index. As shown in Fig. 1, it is clear that the (110) surface is most stable. Furthermore, we have identified the trend that the most stable surface termination has the highest exposition of Sm atoms. This stabilization by the exposition of rare-earth atoms is attributed to the fact that the chemical bonding of 5d states of rare-earth atoms is weaker than that of Fe 3d states. The band energy of 5d states of rare-earth atoms which contribute to the chemical bonding is significantly smaller than that of 3d electrons of Fe atoms as depicted in Fig. 1(e) for the SmFe$_{12}$ bulk. The Mulliken-population analysis revealed that the number of 5d electrons of the Sm atoms is approximately 1.4 while the number of 3d electrons of the Fe atoms is approximately 6.7 for the SmFe$_{12}$ bulk.

Since we expect this trend is universal, we also examine another compound with a rare-earth element and a transition metal, Nd$_2$Fe$_{14}$B. In the case of Nd$_2$Fe$_{14}$B surfaces, the surface-energy density γ is evaluated by

$$\gamma = \frac{E_{\text{slab}} - (N_{\text{Nd}}\mu_{\text{Nd}} + N_{\text{Fe}}\mu_{\text{Fe}} + N_{\text{B}}\mu_{\text{B}})}{2A}. \quad (3)$$

We adopt the condition rich in Nd and Fe and poor in B, where Nd is equilibrium with double hcp (dhcp) Nd as well

as Fe with bcc Fe: $\mu_{\text{Nd}} = \mu_{\text{dhcp-Nd}}$, $\mu_{\text{Fe}} = \mu_{\text{bcc-Fe}}$, and

$$\mu_{\text{B}} = E_{\text{Nd}_2\text{Fe}_{14}\text{B}} - (2\mu_{\text{dhcp-Nd}} + 14\mu_{\text{bcc-Fe}}), \quad (4)$$

where $E_{\text{Nd}_2\text{Fe}_{14}\text{B}}$ is the total energy of the Nd$_2$Fe$_{14}$B bulk per formula unit. By considering all possible 19 terminations, we also identified the most stable termination for the Nd$_2$Fe$_{14}$B(100) surface. Also for this surface, the highest exposition of the rare-earth element, Nd, is seen as depicted in Fig. 2(a). Thus, the (001) and (110) surfaces of Nd$_2$Fe$_{14}$B were examined for only the termination with the highest exposition of Nd atoms. As is clear from Fig. 2(b), the (001) surface is most stable for Nd$_2$Fe$_{14}$B, whereas the next stable surface index is (100).

Next, we discuss local magnetic properties of SmFe$_{12}$(110)/SmCu(100) and SmFe$_{12}$(110)/Fe(001) interfaces. In the case of the interface calculations, we relaxed the lattice parameters for the interface-perpendicular direction in addition to atomic coordinates. For the SmFe$_{12}$(110)/SmCu(100) interface, $\sqrt{2} \times \sqrt{2} \times 1$ SmFe$_{12}$ and $1 \times 1 \times 2$ SmCu were adopted, where the lattice mismatch is approximately 6.4% for the x-axis and 3.3% for the y-axis, respectively. For the SmFe$_{12}$(110)/Fe(100) interface, $\sqrt{2} \times \sqrt{2} \times 3$ SmFe$_{12}$ and $4 \times 5 \times 2$ Fe were adopted, where the lattice mismatch is approximately 5.4% for the x-axis and 0.7% for the y-axis, respectively. Our interface calculations contain up to approximately 550 atoms in the supercell. We evaluate the effective exchange-coupling constant J_{ex} by

$$J_{\text{ex}} = \frac{E_{\text{tot}}^{\text{APMA}} - E_{\text{tot}}^{\text{PMA}}}{2A}, \quad (5)$$

where and $E_{\text{tot}}^{\text{APMA}}$ and $E_{\text{tot}}^{\text{PMA}}$ are the total energy of the optimized interface structures with the antiparallel magnetization alignment (APMA) and the parallel magnetization alignment (PMA) between SmFe$_{12}$ grains, respectively. The total energy $E_{\text{tot}}^{\text{APMA}}$ can be calculated by a supercell doubled in the interface-perpendicular direction as depicted in Fig. 3.

Magnetic moments of the main-phase Fe atoms of each interface and the bulk are shown in Fig. 4(a). In the case of SmFe$_{12}$(110)/SmCu(110) interface, the magnetic moments of

(a)

(b)
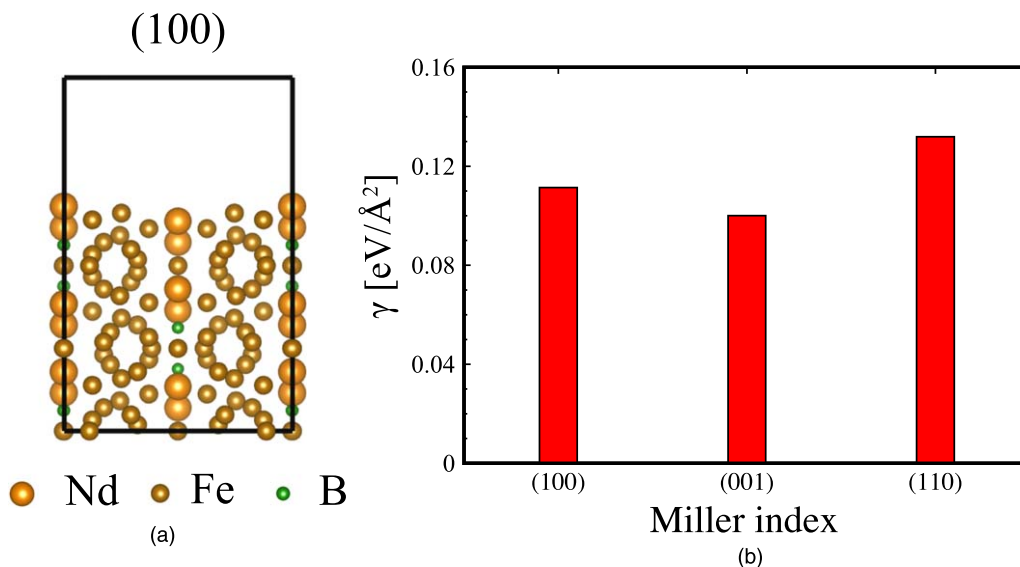
Fig. 2. (Color online) (a) Structure of the (100) surface and (b) surface-energy densities γ of Nd$_2$Fe$_{14}$B.
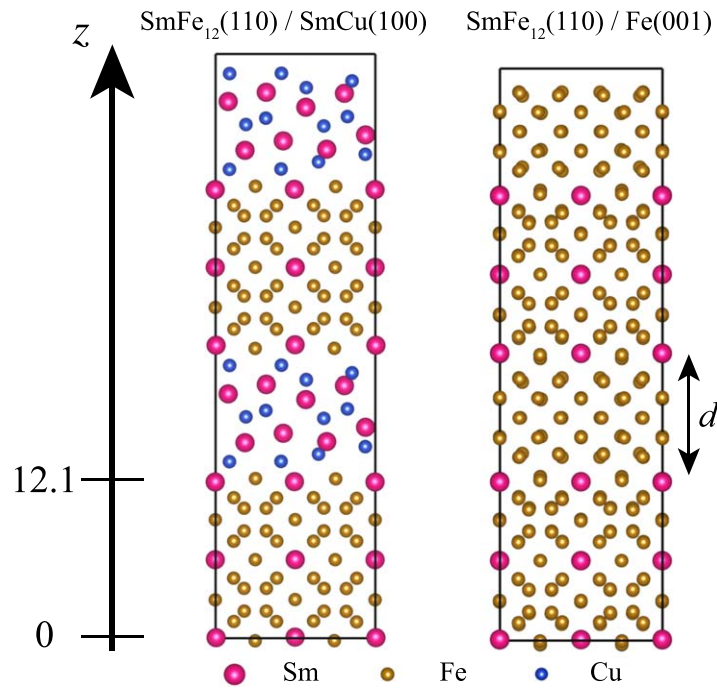
Fig. 3. (Color online) Optimized interface structures. The position with $z = 0$ and 12.1 represents the first interface layer of $SmFe_{12}$. d is the distance between $SmFe_{12}$ grains defined by the first interface layers.
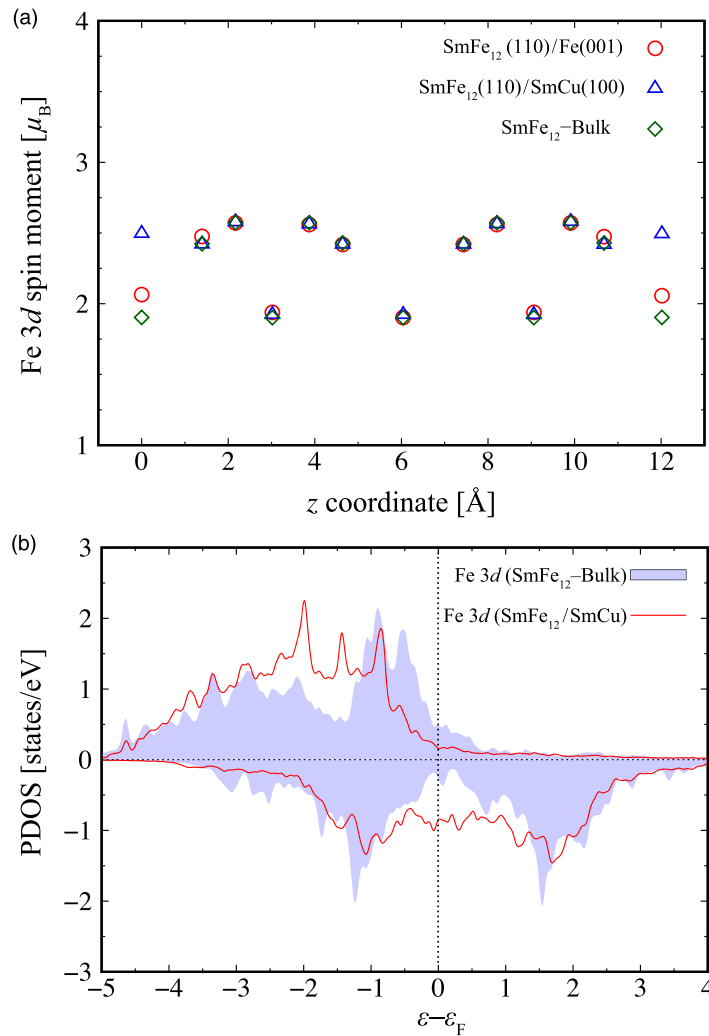
Fig. 4. (Color online) (a) Magnetic moments of the main-phase Fe atoms of each interface and the bulk averaged in the interface-parallel directions (x and y) as a function of the z coordinate. The position with $z = 0$ and 12.1 Å corresponds the first interface layer. (b) The PDOS for $3d$ states of the main-phase Fe atoms located at the interface for the $SmFe_{12}/SmCu$ interface together with that of the $SmFe_{12}$ bulk. The upper (lower) panel denotes the PDOS of the majority (minority) spin, respectively. The single-electron energy is defined relative to the Fermi energy ε_F.
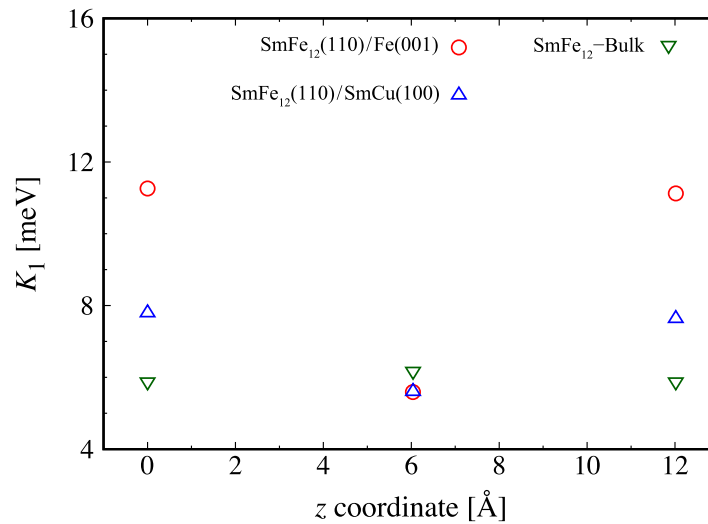
Fig. 5. (Color online) The magnetocrystalline anisotropy constant K_1 of the main-phase Sm atoms of each interface and the $SmFe_{12}$ bulk averaged in the interface-parallel directions (x and y) as a function of the z coordinate. It should be noted that the quantization axis is set as the [001] direction of $SmFe_{12}$, not the direction perpendicular to the interface denoted as z. The position with $z = 0$ and 12.1 Å corresponds the first interface layer.

Table I. Effective exchange-coupling constant J_{ex} and the distance between $SmFe_{12}$ grains d.

Interface	J_{ex} [J m^{-2}]	d [Å]
$SmFe_{12}$(110)/SmCu(100)	0.083	10.29
$SmFe_{12}$(110)/Fe(001)	0.983	9.51

the Fe atoms at the first interface layer ($z = 0$ and $z = 12.1$ Å) greatly increase compared with that of the $SmFe_{12}$ bulk. This enhancement comes from a decrease in the hybridization between $3d$ minority-spin states of the main-phase Fe atoms, which is seen as weakened splitting between bonding and antibonding states in Fig. 4(b). To keep the charge neutrality, the majority spin increases by the amount of the decrease in the minority spin. In addition, the effective exchange-coupling constant J_{ex} is listed in Table I. It is clear that SmCu well suppresses the magnetic interaction between the main-phase grains compared with bcc Fe.

The magnetocrystalline anisotropy constant K_1 of the main-phase Sm atoms is evaluated up to the first order by

$$K_1 = -3J\left(J - \frac{1}{2}\right)\alpha_J A_2^0 \langle r^2 \rangle, \qquad (6)$$

where J, α_J, $\langle r^2 \rangle$, and A_2^0 are the total angular momentum quantum number, the first Stevens factor, the spatial extent of the $4f$ orbitals, and the second-order crystal field coefficient,[25,26] respectively. For Sm^{3+}, $J = 5/2$ ($L = 5$, $S = 5/2$) and $\alpha_J = 13/315$ were adopted. Electronic states of a specific crystal structure determine $A_2^0 \langle r^2 \rangle$ through the expanded radial component of the single-particle effective potential for the spherical harmonics Y_2^0. In evaluating K_1, the quantization axis is set as the [001] direction of $SmFe_{12}$, not the direction perpendicular to the interface denoted as z. As shown in Fig. 5, the stable magnetic direction is always [001] of the main phase ($K_1 > 0$) that is parallel to the (110) interface. The uniaxial anisotropy enhances at the interfaces compared with that of the bulk.

In summary, the most stable surface of $SmFe_{12}$ was determined to be the (110) surface with the highest exposition of Sm atoms from first principles. This trend of the highest

exposition of rare-earth atoms, which comes from weaker chemical bonding of rare-earth $5d$ states compared with that of Fe $3d$ states, was universally observed for $Nd_2Fe_{14}B$ surfaces as well. Moreover, analyzing the magnetic properties of $SmFe_{12}$-based interfaces, we conclude that SmCu is preferred as a subphase of the $SmFe_{12}$-based permanent magnets. Our new findings in this paper will hopefully promote further development of new permanent magnets.

ORCID iDs Yuta Ainai 🆔 https://orcid.org/0000-0003-2741-1179 Yoshihiro Gohda 🆔 https://orcid.org/0000-0002-6047-027X

1) K. Ohashi, T. Yokoyama, R. Osugi, and Y. Tawara, IEEE Trans. Magn. **23**, 3101 (1987).
2) Y. C. Yang, X. D. Zhang, S. L. Ge, Q. Pan, L. S. Kong, H. Li, J. L. Yang, B. S. Zhang, Y. F. Ding, and C. T. Ye, J. Appl. Phys. **70**, 6001 (1991).
3) T. Miyake, K. Terakura, Y. Harashima, H. Kino, and S. Ishibashi, J. Phys. Soc. Jpn. **83**, 043702 (2014).
4) O. Isnard, M. Guillot, S. Miraglia, and D. Fruchart, J. Appl. Phys. **79**, 5542 (1996).
5) L. Bessais and C. Djega-Mariadassou, Phys. Rev. B **63**, 054412 (2001).
6) Y. Hirayama, Y. K. Takahashi, S. Hirosawa, and K. Hono, Scr. Mater. **138**, 62 (2017).
7) N. X. Chen, S. Q. Hao, S. Q. Wu, and J. Shen, J. Magn. Magn. Mater. **223**, 169 (2001).
8) I. Dirba, Y. Harashima, H. Sepehri-Amin, T. Ohkubo, T. Miyake, S. Hirosawa, and K. Hono, J. Alloys Compd. **813**, 152224 (2020).
9) K. H. J. Buschow, J. Magn. Magn. Mater. **100**, 79 (1991).
10) K. Ohashi, Y. Tawara, R. Osugi, J. Sakurai, and Y. Komura, J. Less-Common Met. **139**, L1 (1998).
11) Y. Harashima, T. Fukazawa, H. Kino, and T. Miyake, J. Appl. Phys. **124**, 163902 (2018).
12) Y. Harashima, K. Terakura, H. Kino, S. Ishibashi, and T. Miyake, J. Appl. Phys. **120**, 203904 (2016).
13) Y. C. Yang, B. Kebe, and W. J. James, J. Appl. Phys. **52**, 2077 (1981).
14) D. B. D. Mooij and K. H. J. Buschow, J. Less-Common Met. **136**, 207 (1988).
15) Y. Tatetsu, S. Tsuneyuki, and Y. Gohda, Phy. Rev. Appl. **6**, 064029 (2016).
16) Y. Gohda, Y. Tatetsu, and S. Tsuneyuki, Mater. Trans. **59**, 332 (2018).

17) T. T. Sasaki, Y. Takada, H. Okazaki, T. Ohkubo, T. Nakamura, T. Sato, A. Kato, Y. Kaneko, and K. Hono, J. Alloys Compd. **790**, 750 (2019).

18) I. Dirba, H. Sepehri-Amin, T. Ohkubo, and K. Hono, Acta Mater. **165**, 373 (2019).

19) P. Tozman, H. Sepehri-Amin, Y. K. Takahashi, S. Hirosawa, and K. Hono, Acta Meter. **153**, 354 (2018).

20) D. Ogawa, X. D. Xu, Y. K. Takahashi, T. Ohkubo, S. Hirosawa, and K. Hono, Scr. Mater. **164**, 140 (2019).

21) C. Lu, X. Hong, X. Bao, X. Gao, and J. Zhu, J. Alloys Compd. **784**, 980 (2019).

22) S. Kou, T. Abe, and Y. Gohda, in preparation for publication.

23) T. Ozaki, Phys. Rev. B **67**, 155108 (2003).

24) J. P. Perdew, K. Burke, and M. Ernzerhof, Phys. Rev. Lett. **77**, 3865 (1996).

25) H. Moriya, H. Tsuchiura, and A. Sakuma, J. Appl. Phys. **105**, 07A740 (2009).

26) S. Tanaka, H. Moriya, H. Tsuchiura, A. Sakuma, M. Divis, and P. Novak, J. Appl. Phys. **109**, 07A702 (2011).